

Highlights

Deep neural network method for predicting the iron concentration in silicon solar cell by current-voltage characteristic

Oleg Olikh, Oleg Lozitsky, Oleksii Zavhorodnii

- Research highlights item 1
- Research highlights item 2
- Research highlights item 3

Deep neural network method for predicting the iron concentration in silicon solar cell by current-voltage characteristic

Oleg Olikh^{a,*}, Oleg Lozitsky^a and Oleksii Zavhorodnii^a

^aTaras Shevchenko National University of Kyiv, 64/13, Volodymyrska Street, City of Kyiv, Ukraine, 01601

ARTICLE INFO

Keywords:

Ideality factor

Silicon

n^+-p-p^+ structure

SCAPS

Iron contamination

Machine learning

ABSTRACT

Defect-assisted recombination processes frequently limit the photovoltaic device performance. Non-destructive methods of evaluation of the impurities contamination in solar cells, are important from an applied point of view. In this work, we use numerical device simulation to demonstrate the ability to extract impurity contamination from an ideality factor value and utilizing a deep neural network (DNN). The dense layer DNN was trained by using simulation of current-voltage curves of silicon n^+-p-p^+ structure with the following parameters. The iron concentration ranged from 10^{10} to 10^{13} cm⁻³, the base doping level — from 10^{15} to 10^{17} cm⁻³, the base thickness — from 150 to 240 micron, and the temperature — from 290 to 340 K. The structure with interstitial iron atoms only as well as with coexistence of Fe_iB_s pairs and Fe_i was under consideration. It is shown that DNN is able to predict iron concentration with mean squared relative error up to 0.03.


1. Introduction

Metal contamination control remains an important challenge for silicon processing both for microelectronics, logic technologies and solar cells (SCs) [1, 2, 3, 4]. Typically, metal related defect characterization is performed by Fourier-transform infrared spectroscopy, electron-paramagnetic resonance, minority carrier lifetime measurements, deep level transient spectroscopy (DLTS), Laplace DLTS etc [5, 6, 7]. However, these techniques are time-consuming, require special equipment or/and sample preparing. At the same time, the current-voltage (IV) measurement is a standard rapid industrial SC characterization technique. IV characteristics contain important information about electrically active defects [6, 8]. And a few defect diagnostics by IV characteristics are proposed [6, 8, 9, 10, 11]. The temperature dependencies of current components [10, 11] or IV differential parameters [8, 9] are under consideration. But the numerous and high accuracy IV measurements are required in the first and second cases, respectively.

In our previous work [12], we have shown that the SC ideality factor value (n) can be used to estimate the iron concentration (N_{Fe}). It should be noted that the ideality factor is quite often used to characterize the various semiconductor barrier structures [13, 14, 15, 16, 17]. However, a defect's signature in an ideality factor is convoluted with those from so many other physical processes. As a result the obtained analytic expressions $N_{Fe} = f(n)$ are not general and the numerous grading curves are needed to N_{Fe} determination [12]. On the other hand, in the last decade, the deep learning, which is enable to solve problems without clear algorithmization, have been successfully used in various fields of theoretical and applied physics [18, 19, 20]. Furthermore, materials informatics (combination of material property calculations/measurements and informatics algorithms) has been asserted [21] to become the fourth (along with theory, simulations, and experiments) paradigm of science. The aim of this work is to apply the deep learning approach for predicting the iron concentration from ideality factor (so to say "deep learning for deep levels"). Further, unlike in previous work [12], the back surface field (BSF) n^+-p-p^+ structure was under consideration and the base thickness influence on ideality factor was taken into account as well.

As the approximation to the practical using, the paper considers a fairly simple system which consists of crystalline silicon (c-Si) SC and iron impurity. However, the system is important in practice. Silicon solar cells constitute 90% of current global production capacity [22] and BSF is one of popular designs used for industrial mass production of c-Si SCs [23]. Iron is a major as one of the most detrimental metal impurities in c-Si SCs [2, 3, 4]. The flowchart of the used heuristic approach is shown in Fig. 1. The following milestones can be distinguished. First, the dark IV characteristic is simulated for SCs with both known contaminant composition and various parameters. In our numerical simulation

*Corresponding author

 olegolikh@knu.ua (Oleg Olikh)

ORCID(s):

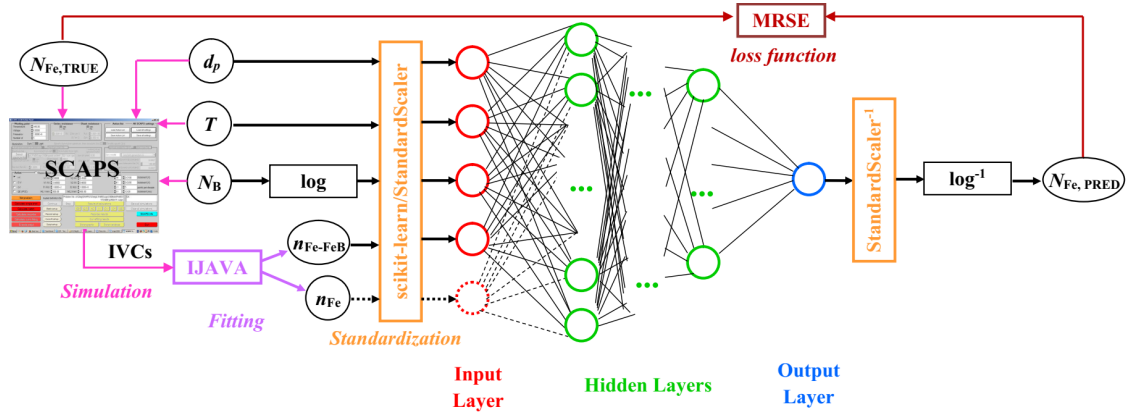


Figure 1: Schematic of deep learning based approach for predicting the iron concentration. Additional details are discussed in the body of the article.

we make use of SCAPS-1D [24, 25], which widely used to model silicon-based devices [26, 27, 28]. Second, the obtained characteristic is fitted according to the double-diode model and the ideality factor is estimated. As a result of aforesaid steps, the labeled datasets were produced. Obviously, the labeled dataset from experimental IVs would be preferable, but it is practically difficult to find the thousands of samples with the required parameters. Third, the training of deep neural network (DNN) to estimate an iron contamination by using SC's base thickness, doping level, temperature, and ideality factor value. Fours, the DNN testing.

2. Simulation Details

The presented calculation uses n^+p-p^+ structure. n^+ is the emitter layer with the donor concentration $N_D = 10^{19} \text{ cm}^{-3}$ and the thickness $0.5 \text{ } \mu\text{m}$. p and p^+ are the base and BSF-layer, respectively, which are uniformly doped with boron. $1 \text{ } \mu\text{m}$ and $5 \times 10^{18} \text{ cm}^{-3}$ are the thickness d_{BSF} and the acceptor concentration N_{BSF} of the p^+ layer. The base with the thickness $d_p = 150\text{--}240 \text{ } \mu\text{m}$ is doped with concentration $N_B = 10^{15}\text{--}10^{17} \text{ cm}^{-3}$.

The simulations were carried out over the temperature range $290\text{--}340 \text{ K}$. The SCAPS setting file was created for each temperature using the following material parameters. The bandgap E_G and bandgap narrowing ΔE_G models are, respectively, from Pässler [29] and Yan and Cuevas [30]:

$$E_G = E_{G0} - \alpha \Theta \left\{ \frac{1 - 3\Delta^2}{e^{\frac{\Theta}{T}} - 1} + \frac{3\Delta^2}{2} \left(\sqrt{1 + \frac{\pi^2}{3(1+\Delta^2)} \left(\frac{2T}{\Theta} \right)^2} + \frac{3\Delta^2 - 1}{4} \left(\frac{2T}{\Theta} \right)^3 + \frac{8}{3} \left(\frac{2T}{\Theta} \right)^4 + \left(\frac{2T}{\Theta} \right)^6 - 1 \right) \right\}, \quad (1)$$

$$\Delta E_G = 4.20 \times 10^{-5} \left[\ln \left(\frac{N_D}{10^{14}} \right) \right]^3; \quad \Delta E_G = 4.72 \times 10^{-5} \left[\ln \left(\frac{N_{B,BSF}}{10^{14}} \right) \right]^3, \quad (2)$$

where $E_{G0} = 1.1701 \text{ eV}$, $\alpha = 3.23 \times 10^{-4} \text{ eV/K}$, $\Theta = 446 \text{ K}$, $\Delta = 0.51$. The carrier thermal velocities are calculated from models by Green [31]:

$$v_{th,n} = \sqrt{\frac{8qkT}{0.28m_0\pi}}; \quad v_{th,p} = \sqrt{\frac{8qkT}{0.41m_0\pi}}, \quad (3)$$

where m_0 is the free electron mass. The effective states density masses in the conduction band m_{dC}^* and the valence band m_{dV}^* are calculated according to models from Couderc et al. [32]:

$$\left(\frac{m_{dC}^*}{m_0} \right)^{1.5} = 1.094 - 1.312 \times 10^{-5}T + 6.753 \times 10^{-7}T^2 + 4.609 \times 10^{-10}T^3, \quad (4)$$

$$\left(\frac{m_{dV}^*}{m_0}\right)^{1.5} = 0.3426 + 3.376 \times 10^{-3}T - 4.689 \times 10^{-6}T^2 + 2.525 \times 10^{-9}T^3. \quad (5)$$

The carrier mobilities and the free carrier effective masses are from Klaassen [33] and O'Mara et al. [34], respectively. The temperature and doping dependencies of Auger recombination coefficients are calculated from models by Altermatt et al. [35]:

$$C_p(T) = (7.91 \times 10^{-32} - 4.13 \times 10^{-35}T + 3.59 \times 10^{-37}T^2) \times \left(1 + (564812T^{-1.6545} - 1) \left(1 - \tanh \left[\left\{\frac{p}{5 \times 10^{16}}\right\}^{0.29}\right]\right)\right), \quad (6)$$

$$C_n(T) = 2.8 \times 10^{-31} \times \left(1 + (235548T^{-1.5013} - 1) \left(1 - \tanh \left[\left\{\frac{n}{5 \times 10^{16}}\right\}^{0.34}\right]\right)\right). \quad (7)$$

The Auger recombination coefficient is from Nguyen et al. [36].

The outside surface recombination with electron and hole velocities 10^3 cm/s was taken into account.

The simulations are carried out under the assumption that the defect-assisted recombination is connected with iron-related deep levels only. As the base and the SBF-layer uniform contaminant, iron is assumed to be in concentration $N_{\text{Fe}} = 10^{10}$ – 10^{13} cm⁻³. The simulations have been performed for the following two cases. In the first one, the concentration of totally dissolved iron is given by a sum of the concentration of the interstitial iron Fe_i and the concentration of trigonal iron-boron pair Fe_iB_s :

$$N_{\text{Fe}} = N_{\text{Fe}_i} + N_{\text{Fe}_i\text{B}_s}. \quad (8)$$

The defect distributions are uniform, depend on the Fermi level F position, and are given by [37, 38]:

$$\frac{N_{\text{FeB}}}{N_{\text{Fe}}} = \frac{N_{\text{B}} 10^{-23} \exp\left(-\frac{E_b}{kT}\right)}{\left[1 + \frac{N_{\text{B}}}{10^{23}} \exp\left(-\frac{E_b}{kT}\right)\right] \left[1 + \exp\left(-\frac{F-E_{\text{Fe}_i}}{kT}\right)\right]}, \quad N_{\text{Fe}_i} = N_{\text{Fe}} - N_{\text{FeB}}, \quad (9)$$

where $E_b = 0.582$ eV is the binding energy of the Fe_iB_s pairs, E_{Fe_i} is the donor level, associated with Fe_i . This case correspond to the equilibrium condition and is labeled “Fe-FeB” from now on.

In the second one, the Fe_i is suggested to be only present with uniform distribution ($N_{\text{Fe}_i} = N_{\text{Fe}}$). This case can be realized by heat treatment (210°C, 3 min) [39] or intense illumination [40] and is referred as “Fe-FeB” hereafter.

The donor level $E_{\text{Fe}_i} = E_V + 0.394$ eV with electron $\sigma_{n,\text{Fe}} = 3.47 \times 10^{-11}T^{-1.48}$ cm² and hole $\sigma_{p,\text{Fe}} = 4.54 \times 10^{-16} \exp\left(-\frac{0.05}{kT}\right)$ cm² capture cross-sections [37, 41] is associated with Fe_i in simulations. The donor level $E_{\text{FeB}}^{\text{D}} = E_V + 0.10$ eV, $\sigma_{n,\text{FeB}}^{\text{D}} = 4 \times 10^{-13}$ cm², $\sigma_{p,\text{FeB}}^{\text{D}} = 2 \times 10^{-14}$ cm² and acceptor level $E_{\text{FeB}}^{\text{A}} = E_C - 0.26$ eV, $\sigma_{n,\text{FeB}}^{\text{A}} = 5.1 \times 10^{-9}T^{-2.5}$ cm², $\sigma_{p,\text{FeB}}^{\text{A}} = 3.32 \times 10^{-10} \exp\left(-\frac{0.262}{kT}\right)$ cm² [42, 37, 41] are used for Fe_iB_s .

The dark forward IV characteristic were generated by SCAPS over a voltage range up to 0.45 V. According to the two-diode model, the dark SC current is given by [43]

$$I = I_{01} \left[\exp\left(-\frac{q(V - R_s I)}{kT}\right) - 1 \right] + I_{02} \left[\exp\left(-\frac{q(V - R_s I)}{nkT}\right) - 1 \right] + \frac{V - R_s I}{R_{sh}}, \quad (10)$$

where I_{01} and I_{02} are the saturation currents, R_{sh} and R_s are the shunt and series resistances. The two-diode model are often used to describe real Si SCs and we used Eq. 10 to fit the simulated data by taking n , I_{01} , I_{02} , R_{sh} , and R_s as fitting parameters. The fitting was performed by using the meta-heuristic method IJAVA [44]. It should be noted that influence of both R_s (obtained values $< 10^{-2}$ Ω) and R_{sh} (obtained values $> 10^{18}$ Ω) can be neglected in simulated IV.

It is the ideality factor value n which is used in our further calculation. The ideality factors, which are obtained in Fe-case and Fe-FeB-case, are referred as n_{Fe} and $n_{\text{Fe-FeB}}$ hereafter. The typical simulated dependencies of the ideality factor are shown in Fig. 2. The detailed discussion about n_{Fe} and $n_{\text{Fe-FeB}}$ values are presented elsewhere [45], however it should be noted that (i) n can takes equal values for different SC parameters values; (ii) dependencies of n_{Fe} and $n_{\text{Fe-FeB}}$ varies slightly.

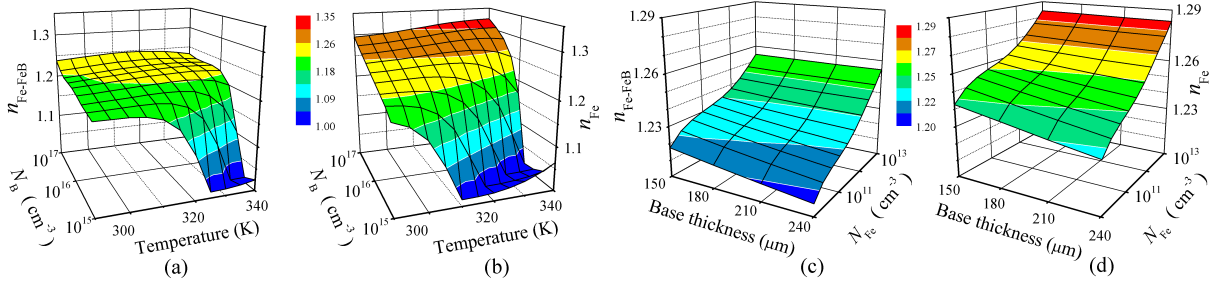


Figure 2: Ideality factor versus temperature and boron concentration (a, b) or base thickness and iron concentration (c, d). The Fe-FeB-case (a, c) and Fe-case (b, d). $N_{\text{Fe}} = 10^{10} \text{ cm}^{-3}$ (a, b), $d_p = 180 \mu\text{m}$ (a, b), $N_B = 10^{16} \text{ cm}^{-3}$ (c, d), $T = 320 \text{ K}$ (c, d).

3. Deep neural network models

Training a deep neural network requires a large number of samples. In order to build a training dataset, we used IV characteristics, which are simulated by using 4 d_p values, 9 N_B values, 11 T values and 19 N_{Fe} values. These base thickness, doping level, temperature, and iron concentration values are regularly (for T and d_p in linear scale, for N_{Fe} and N_B in logarithmic scale) distributed over the ranges 150–240 μm , 10^{15} – 10^{17} cm^{-3} , 290 – 340 K, and 10^{10} – 10^{13} cm^{-3} , respectively. Thus, 7524 IV characteristics are simulated in Fe-case as well as in Fe-FeB-case to build a training dataset.

Besides, several test datasets are prepared. The d_p , N_B , and N_{Fe} values, which equal to values from training dataset, and T values, which is divergent from training dataset, are used to build the test dataset, labeled “T-varied”. These dataset is based on 894 pairs of IV characteristics. The similar approach was used to prepare “d-varied” (1189 samples), “Fe-varied” (856 samples), and “B-varied” (514 samples) test datasets. The base thickness, doping level, temperature, and iron concentration values, which are divergent from training dataset values, are used to prepare “All-varied” (684 samples).

The precise parameters values are listed in Supplementary Material.

We have tried to construct the DNN, which is able to estimate iron contamination by using SC parameters (d_p and N_B), measurement temperature, and result of IV fitting (ideality factor value). As it is shown in Fig. 1 two DNNs with different input parameters were under consideration. The input sample of the first one consist of $\{d_p, \log N_B, T, n_{\text{Fe-FeB}}\}$. In practice, these input set can be obtained from one dark IV measurement. These neural network referred as $\text{DNN}_{\text{FeFeB}}$ hereafter. The second one uses $\{d_p, \log N_B, T, n_{\text{Fe-FeB}}, n_{\text{Fe}}\}$ in input layer. In practice, the obtaining of such a set requires additional SC processing (e.g. intense illumination) and two IV measuring. The label $\text{DNN}_{\text{FeFeB-Fe}}$ is used below.

The dense deep neural network was implemented through the high-level Keras API provided by TensorFlow [46]. The input layers consist of 4 or 5 nodes — see Fig. 1. 1 node and linear activation were used in output layer. The five configurations of hidden layers were under consideration: (i) “pipe”: each hidden layer contains equal number of nodes; (ii) “trapezium”: six hidden layers, number of neural linearly decreases from 100% (first layer) to 50% (last layer); (iii) “triangle”: ten layers, number of neural linearly decreases from 100% (first layer) to 10% (last layer); (iv) “butterfly”: two serial reflected trapezium configurations; (v) “fir”: two serial trapezium configurations.

The loss function was chosen mean squared relative error (MSRE):

$$\text{MSRE} = \frac{1}{N_s} \sum_{i=1}^{N_s} \frac{(N_{\text{Fe,TRUE},i} - N_{\text{Fe,PRED},i})^2}{N_{\text{Fe,TRUE},i} \cdot N_{\text{Fe,PRED},i}}, \quad (11)$$

where N_s is the number of samples in dataset, $N_{\text{Fe,TRUE},i}$ is the iron concentration, which was used in simulation of i -th sample, $N_{\text{Fe,PRED},i}$ is the DNN prediction for i -th sample.

Hyperparameters include the number of nodes for first hidden layer, the number of hidden layers (in pipe configuration), the batch size, the activation function, the optimizer, the learning rate, the preprocessing method, the dropout rate, the regularization function, the regularization rate, and the weight initializer. A grid search (coarse tuning) and Bayesian search (fine tuning) were performed over the predefined hyperparameter space, shown in Table 1, and the

best hyperparameter combination is chosen.

Table 1

Hyperparameter space for DNNs.

Hyperparameter	Values
# nodes for first hidden layer	30, 40, 50, 75, 100, 120, 150
# hidden layers	4, 5, 6, 8, 10, 15
batch size	8, 16, 32, 64, 128
activation function	ReLU, sigmoid, tanh, SELU, ELU
optimizer	SGD, RMSprop, Adam, Adadelta, Adagrad, Adamax, Nadam, Ftrl
learning rate	10^{-5} , 10^{-4} , 10^{-3} , 10^{-2}
epoch	100, 300, 400, 600, 1000, 1500
preprocessing method	StandartScaler, MinMaxScaler
regularization function	None, L2, L1, Dropout
regularization rate	10^{-5} , 10^{-4} , 10^{-3} , 10^{-2}
dropout rate	0.2, 0.3, 0.4, 0.5
weight initializer	Xavier Normal or Uniform, He Normal or Uniform, Random Normal or Uniform, Ones

10-fold cross-validation was used to estimate DNN training. The MSRE, determination coefficient R^2 , and correlation coefficient R were three metrics used to evaluate the performance of the DNN models on test datasets.

4. Results and discussion

Table 2

Chosen hyperparameter combinations.

Hyperparameter	DNN _{FeFeB}	DNN _{FeFeB-Fe}
# nodes for hidden layers	120, 108, 96, 84, 72, 60	100, 100, 100, 100
batch size	32	32
activation function	ReLU	ELU
optimizer	Adamax	Adamax
learning rate	10^{-3}	10^{-3}
epoch	400	1500
preprocessing method	StandartScaler	StandartScaler
regularization function	None	None
weight initializer	Xavier Normal	Xavier Normal

Table 3

Results of 10-fold cross-validation

Dataset	DNN _{FeFeB}	MSRE	DNN _{FeFeB-Fe}
training	0.31 ± 0.07		0.03 ± 0.01
full	0.28 ± 0.05		0.03 ± 0.01

As a result of aforesaid steps, the labeled datasets were produced.

The Elsevier cas-sc class is based on the standard article class and supports almost all of the functionality of that class. In addition, it features commands and options to format the

- document style
- baselineskip

Table 4
DNN's testing results

Dataset	MSRE	DNN _{FeFeB} R^2	R	MSRE	DNN _{FeFeB-Fe} R^2	R
T-varied	0.41	0.936	0.967	0.020	0.994	0.997
d-varied	0.37	0.961	0.980	0.018	0.996	0.998
B-varied	1.06	0.881	0.939	0.084	0.991	0.995
Fe-varied	0.06	0.991	0.996	0.005	0.999	0.999
All-varied	0.54	0.813	0.901	0.138	0.948	0.974

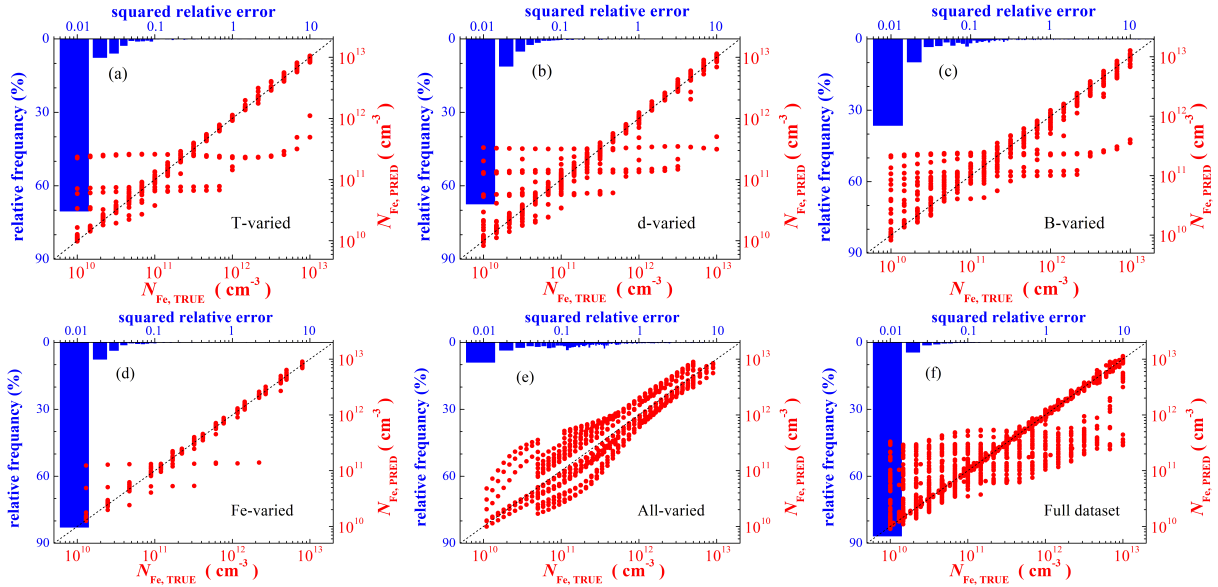


Figure 3: Iron concentrations are plotted against those generated by DNN_{FeFeB-Fe} on T-varied (a), d-varied (b), B-varied (c), Fe-varied (d), All-varied (e), and full (f) datasets (red points). Bars represent histograms of squared relative error. DNN was learned by training (a)–(e) or full (f) dataset. The black dashed lines are the identity lines serving as the references.

- front matter
- keywords and MSC codes
- theorems, definitions and proofs
- tables of enumerations
- citation style and labeling.

This class depends on the following packages for its proper functioning:

1. natbib.sty for citation processing;
2. geometry.sty for margin settings;
3. fleqn.clo for left aligned equations;
4. graphicx.sty for graphics inclusion;
5. hyperref.sty optional packages if hyperlinking is required in the document;

All the above packages are part of any standard L^AT_EX installation. Therefore, the users need not be bothered about downloading any extra packages.

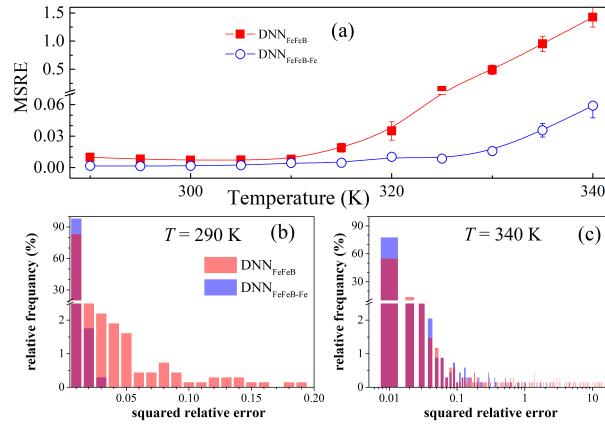


Figure 4: Iron concentrations are plotted against those generated by $DNN_{FeFeB-Fe}$ on T-varied (a), d-varied (b), B-varied (c), Fe-varied (d), All-varied (e), and full (f) datasets (red points). Bars represent histograms of squared relative error. DNN was learned by training (a)–(e) or full (f) dataset. The black dashed lines are the identify lines serving as the references.

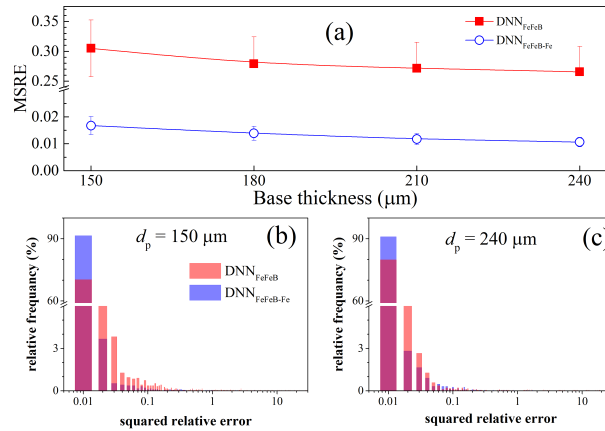


Figure 5: Iron concentrations are plotted against those generated by $DNN_{FeFeB-Fe}$ on T-varied (a), d-varied (b), B-varied (c), Fe-varied (d), All-varied (e), and full (f) datasets (red points). Bars represent histograms of squared relative error. DNN was learned by training (a)–(e) or full (f) dataset. The black dashed lines are the identify lines serving as the references.

5. Installation

The package is available at author resources page at Elsevier (<http://www.elsevier.com/locate/latex>). The class may be moved or copied to a place, usually, $\$TEXMF/tex/latex/elsevier/$, or a folder which will be read by \LaTeX during document compilation. The \TeX file database needs updation after moving/copying class file. Usually, we use commands like `mktexlsr` or `texhash` depending upon the distribution and operating system.

6. Front matter

The author names and affiliations could be formatted in two ways:

- (1) Group the authors per affiliation.
- (2) Use footnotes to indicate the affiliations.

See the front matter of this document for examples. You are recommended to conform your choice to the journal you are submitting to.

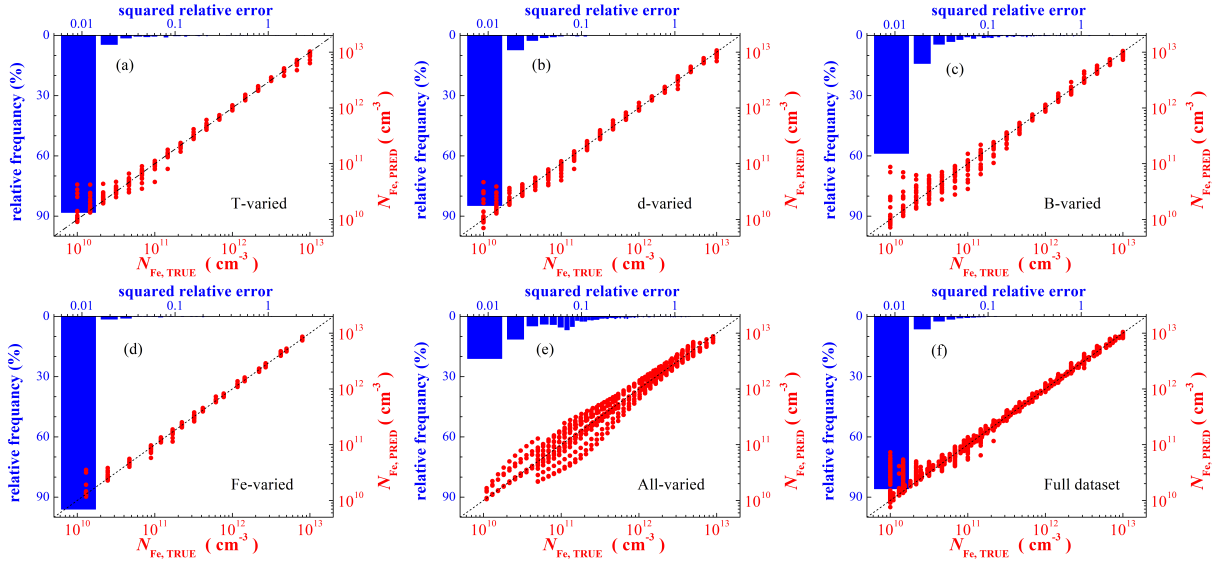


Figure 6: Iron concentrations are plotted against those generated by $\text{DNN}_{\text{FeFeB}}$ on T-varied (a), d-varied (b), B-varied (c), Fe-varied (d), All-varied (e), and full (f) datasets (red points). Bars represent histograms of squared relative error. DNN was learned by training (a)–(e) or full (f) dataset. The black dashed lines are the identity lines serving as the references.

7. Bibliography styles

There are various bibliography styles available. You can select the style of your choice in the preamble of this document. These styles are Elsevier styles based on standard styles like Harvard and Vancouver. Please use Bib \LaTeX to generate your bibliography and include DOIs whenever available.

8. Floats

Figures may be included using the command, `\includegraphics` in combination with or without its several options to further control graphic. `\includegraphics` is provided by `graphic[s,x].sty` which is part of any standard \LaTeX distribution. `graphicx.sty` is loaded by default. \LaTeX accepts figures in the postscript format while pdf\LaTeX accepts *.pdf, *.mps (metapost), *.jpg and *.png formats. pdf\LaTeX does not accept graphic files in the postscript format.

The `table` environment is handy for marking up tabular material. If users want to use `multirow.sty`, `array.sty`, etc., to fine control/enhance the tables, they are welcome to load any package of their choice and `cas-sc.cls` will work in combination with all loaded packages.

Table 5

This is a test caption. This is a test caption. This is a test caption. This is a test caption.

Col 1	Col 2	Col 3	Col 4
12345	12345	123	12345
12345	12345	123	12345
12345	12345	123	12345
12345	12345	123	12345
12345	12345	123	12345

9. Theorem and theorem like environments

`cas-sc.cls` provides a few shortcuts to format theorems and theorem-like environments with ease. In all commands

the options that are used with the `\newtheorem` command will work exactly in the same manner. `cas-sc.cls` provides three commands to format theorem or theorem-like environments:

```
\newtheorem{theorem}{Theorem}
\newtheorem{lemma}[theorem]{Lemma}
\newdefinition{rmk}{Remark}
\newproof{pf}{Proof}
\newproof{pot}{Proof of Theorem \ref{thm2}}
```

The `\newtheorem` command formats a theorem in L^AT_EX's default style with italicized font, bold font for theorem heading and theorem number at the right hand side of the theorem heading. It also optionally accepts an argument which will be printed as an extra heading in parentheses.

```
\begin{theorem}
  For system (8), consensus can be achieved with
   $\|T_{\omega z}\| \dots$ 
  \begin{eqnarray}\label{10}
    \dots
  \end{eqnarray}
\end{theorem}
```

Theorem 1. *For system (8), consensus can be achieved with $\|T_{\omega z}\| \dots$*

....

(12)

The `\newdefinition` command is the same in all respects as its `\newtheorem` counterpart except that the font shape is roman instead of italic. Both `\newdefinition` and `\newtheorem` commands automatically define counters for the environments defined.

The `\newproof` command defines proof environments with upright font shape. No counters are defined.

10. Enumerated and Itemized Lists

`cas-sc.cls` provides an extended list processing macros which makes the usage a bit more user friendly than the default L^AT_EX list macros. With an optional argument to the `\begin{enumerate}` command, you can change the list counter type and its attributes.

```
\begin{enumerate}[1.]
\item The enumerate environment starts with an optional
  argument '1.', so that the item counter will be suffixed
  by a period.
\item You can use 'a)' for alphabetical counter and '(i)' for
  roman counter.
\begin{enumerate}[a)]
  \item Another level of list with alphabetical counter.
  \item One more item before we start another.
  \item One more item before we start another.
  \item One more item before we start another.
  \item One more item before we start another.
\end{enumerate}
```

Further, the enhanced list environment allows one to prefix a string like 'step' to all the item numbers.

```
\begin{enumerate}[Step 1.]
\item This is the first step of the example list.
\item Obviously this is the second step.
\item The final step to wind up this example.
\end{enumerate}
```

11. Cross-references

In electronic publications, articles may be internally hyperlinked. Hyperlinks are generated from proper cross-references in the article. For example, the words Fig. 1 will never be more than simple text, whereas the proper cross-reference `\ref{tiger}` may be turned into a hyperlink to the figure itself: Fig. 1. In the same way, the words Ref. [1] will fail to turn into a hyperlink; the proper cross-reference is `\cite{Knuth96}`. Cross-referencing is possible in \LaTeX for sections, subsections, formulae, figures, tables, and literature references.

12. Bibliography

Two bibliographic style files (*.bst) are provided — `model1-num-names.bst` and `model2-names.bst` — the first one can be used for the numbered scheme. This can also be used for the numbered with new options of `natbib.sty`. The second one is for the author year scheme. When you use `model2-names.bst`, the citation commands will be like `\citep`, `\citet`, `\citealt` etc. However when you use `model1-num-names.bst`, you may use only `\cite` command.

the `bibliography` environment. Each reference is a `\bibitem` and each `\bibitem` is identified by a label, by which it can be cited in the text:

In connection with cross-referencing and possible future hyperlinking it is not a good idea to collect more than one literature item in one `\bibitem`. The so-called Harvard or author-year style of referencing is enabled by the \LaTeX package `natbib`. With this package the literature can be cited as follows:

- Parenthetical: `\citep{WB96}` produces (Wettig & Brown, 1996).
- Textual: `\citet{ESG96}` produces Elson et al. (1996).
- An affix and part of a reference: `\citep[e.g.][Ch. 2]{Gea97}` produces (e.g. Governato et al., 1997, Ch. 2).

In the numbered scheme of citation, `\cite{<label>}` is used, since `\citep` or `\citet` has no relevance in the numbered scheme. `natbib` package is loaded by `cas-sc` with `numbers` as default option. You can change this to author-year or harvard scheme by adding option `authoryear` in the class loading command. If you want to use more options of the `natbib` package, you can do so with the `\biboptions` command. For details of various options of the `natbib` package, please take a look at the `natbib` documentation, which is part of any standard \LaTeX installation.

A. My Appendix

Appendix sections are coded under `\appendix`.

`\printcredits` command is used after appendix sections to list author credit taxonomy contribution roles tagged using `\credit` in frontmatter.

CRedit authorship contribution statement

Oleg Olikh: Conceptualization, Methodology, Formal analysis, Data Curation, Writing - Review & Editing, Visualization, Supervision. **Oleg Lozitsky:** Software, Validation, Investigation, Writing - Original Draft. **Oleksii Zavorodnii:** Software, Validation, Formal analysis, Writing - Original Draft.

Data availability

The simulated IV characteristics, n_{Fe} and $n_{\text{Fe-FeB}}$ values, and trained DNNs are available at <https://github.com/olegolikh/IVcharacteristics.git>.

Declaration of competing interest

The authors declare that they have no known competing financial interests or personal relationships that could have appeared to influence the work reported in this paper.

Acknowledgment

This work was supported by National Research Foundation of Ukraine (project number 2020.02/0036)

References

- [1] C. Claeys, E. Simoen, Metal Impurities in Silicon- and Germanium-Based Technologies: Origin, Characterization, Control, and Device Impact, volume 270 of *Springer Series in Materials Science*, Springer International Publishing, Berlin/New York, 2018.
- [2] H. Zhu, X. Yu, X. Zhu, Y. Wu, J. He, J. Vanhellemont, D. Yang, Low temperature iron gettering by grown-in defects in p-type Czochralski silicon, *Superlattices Microstruct.* 99 (2016) 192–196.
- [3] J. Schmidt, Effect of dissociation of iron–boron pairs in crystalline silicon on solar cell properties, *Progress in Photovoltaics: Research and Applications* 13 (2005) 325–331.
- [4] M. Schubert, M. Padilla, B. Michl, L. Mundt, J. Giesecke, J. Hohl-Ebinger, J. Benick, W. Warta, M. Tajima, A. Ogura, Iron related solar cell instability: Imaging analysis and impact on cell performance, *Sol. Energy Mater. Sol. Cells* 138 (2015) 96–101.
- [5] D. K. Schroder, *Semiconductor Material and Device Characterization*, John Wiley & Sons, New Jersey, third edition, 2006.
- [6] R. C. Kurchin, J. R. Poindexter, V. Vähänissi, H. Savin, C. del Cañizo, T. Buonassisi, How much physics is in a current-voltage curve? inferring defect properties from photovoltaic device measurements, *IEEE J. Photovolt.* 10 (2020) 1532–1537.
- [7] A. R. Peaker, V. P. Markevich, J. Coutinho, Tutorial: Junction spectroscopy techniques and deep-level defects in semiconductors, *J. Appl. Phys.* 123 (2018) 161559.
- [8] S. V. Bulyarskiy, A. V. Lakalin, M. A. Saurov, G. G. Gusarov, The effect of vacancy-impurity complexes in silicon on the current-voltage characteristics of p-n junctions, *J. Appl. Phys.* 128 (2020) 155702.
- [9] S. V. Bulyarskiy, The effect of electron-phonon interaction on the formation of reverse currents of p-n-junctions of silicon-based power semiconductor devices, *Solid-State Electron.* 160 (2019) 107624.
- [10] C. Claeys, E. Simoen, Device performance as a metrology tool to detect metals in silicon, *physica status solidi (a)* 216 (2019) 1900126.
- [11] E. Simoen, C. Claeys, J. Vanhellemont, Defect analysis in semiconductor materials based on p-n junction diode characteristics, in: *Defects and Diffusion in Semiconductors - An Annual Retrospective IX*, volume 261 of *Defect and Diffusion Forum*, Trans Tech Publications Ltd, 2007, pp. 1–24.
- [12] O. Olikh, Relationship between the ideality factor and the iron concentration in silicon solar cells, *Superlattices Microstruct.* 136 (2019) 106309.
- [13] A. S. H. van der Heide, A. Schonecker, J. H. Bultman, W. C. Sinke, Explanation of high solar cell diode factors by nonuniform contact resistance, *Progress in Photovoltaics: Research and Applications* 13 (2005) 3–16.
- [14] L. Duan, H. Yi, C. Xu, M. B. Upama, M. A. Mahmud, D. Wang, F. H. Shabab, A. Uddin, Relationship between the diode ideality factor and the carrier recombination resistance in organic solar cells, *IEEE Journal of Photovoltaics* 8 (2018) 1701–1709.
- [15] J. Chen, M. Zhu, X. Lu, X. Zou, Electrical characterization of GaN Schottky barrier diode at cryogenic temperatures, *Appl. Phys. Lett.* 116 (2020) 062102.
- [16] P. Dalapati, N. Manik, A. Basu, Analysis of the temperature dependence of diode ideality factor in InGaN-based UV-A light-emitting diode, *Semiconductors* 54 (2020) 1284–1289.
- [17] P. Calado, D. Burkitt, J. Yao, J. Troughton, T. M. Watson, M. J. Carnie, A. M. Telford, B. C. O'Regan, J. Nelson, P. R. Barnes, Identifying dominant recombination mechanisms in perovskite solar cells by measuring the transient ideality factor, *Phys. Rev. Applied* 11 (2019) 044005.
- [18] G. Carleo, I. Cirac, K. Cranmer, L. Daudet, M. Schuld, N. Tishby, L. Vogt-Maranto, L. Zdeborová, Machine learning and the physical sciences, *Rev. Mod. Phys.* 91 (2019) 045002.
- [19] S. Ju, S. Shimizu, J. Shiomi, Designing thermal functional materials by coupling thermal transport calculations and machine learning, *J. Appl. Phys.* 128 (2020) 161102.
- [20] S. Rodrigues, H. G. Ramos, F. Morgado-Dias, Machine learning pv system performance analyser, *Prog. Photovoltaics Res. Appl.* 26 (2018) 675–687.
- [21] S. Ju, S. Shimizu, J. Shiomi, Designing thermal functional materials by coupling thermal transport calculations and machine learning, *J. Appl. Phys.* 128 (2020) 161102.
- [22] J. Jean, P. R. Brown, R. L. Jaffe, T. Buonassisi, V. Bulović, Pathways for solar photovoltaics, *Energy Environ. Sci.* 8 (2015) 1200–1219.
- [23] J. Ajayan, D. Nirmal, P. Mohankumar, M. Saravanan, M. Jagadesh, L. Arivazhagan, A review of photovoltaic performance of organic/inorganic solar cells for future renewable and sustainable energy technologies, *Superlattices Microstruct.* 143 (2020) 106549.
- [24] M. Burgelman, P. Nollet, S. Degraeve, Modelling polycrystalline semiconductor solar cells, *Thin Solid Films* 361–362 (2000) 527–532.
- [25] K. Decock, S. Khelifi, M. Burgelman, Modelling multivalent defects in thin film solar cells, *Thin Solid Films* 519 (2011) 7481–7484.
- [26] E. Hu, G. Yue, R. Zhang, Y. Zheng, L. Chen, S. Wang, Numerical simulations of multilevel impurity photovoltaic effect in the sulfur doped crystalline silicon, *Renewable Energy* 77 (2015) 442–446.
- [27] A. Hamache, N. Sengouga, A. Meftah, M. Henini, Modeling the effect of 1 MeV electron irradiation on the performance of n^+p silicon space solar cells, *Radiat. Phys. Chem.* 123 (2016) 103–108.
- [28] K. Kim, J. Gwak, S. K. Ahn, Y.-J. Eo, J. H. Park, J.-S. Cho, M. G. Kang, H.-E. Song, J. H. Yun, Simulations of chalcopyrite/c-si tandem cells using scaps-1d, *Sol. Energy* 145 (2017) 52–58.
- [29] R. Pässler, Dispersion-related description of temperature dependencies of band gaps in semiconductors, *Phys. Rev. B* 66 (2002) 085201.
- [30] D. Yan, A. Cuevas, Empirical determination of the energy band gap narrowing in p^+ silicon heavily doped with boron, *J. Appl. Phys.* 116 (2014) 194505.
- [31] M. A. Green, Intrinsic concentration, effective densities of states, and effective mass in silicon, *J. Appl. Phys.* 67 (1990) 2944–2954.
- [32] R. Couderc, M. Amara, M. Lemi, Reassessment of the intrinsic carrier density temperature dependence in crystalline silicon, *J. Appl. Phys.* 115 (2014) 093705.
- [33] D. Klaassen, A unified mobility model for device simulation — I. model equations and concentration dependence, *Solid-State Electron.* 35 (1992) 953–959.
- [34] W. O'Mara, R. Herring, L. Hant, *Handbook of semiconductor silicon technology*, Noyes Publications, New Jersey, USA, 1990.
- [35] P. P. Altermatt, J. Schmidt, G. Heiser, A. G. Aberle, Assessment and parameterisation of Coulomb-enhanced Auger recombination coefficients

- in lowly injected crystalline silicon, J. Appl. Phys. 82 (1997) 4938–4944.
- [36] H. T. Nguyen, S. C. Baker-Finch, D. Macdonald, Temperature dependence of the radiative recombination coefficient in crystalline silicon from spectral photoluminescence, Appl. Phys. Lett. 104 (2014) 112105.
 - [37] J. D. Murphy, K. Bothe, M. Olmo, V. V. Voronkov, R. J. Falster, The effect of oxide precipitates on minority carrier lifetime in p-type silicon, J. Appl. Phys. 110 (2011) 053713.
 - [38] W. Wijaranakula, The reaction kinetics of iron–boron pair formation and dissociation in p-type silicon, J. Electrochem. Soc. 140 (1993) 275–281.
 - [39] G. Zoth, W. Bergholz, A fast, preperetion-free method to detect irpn in silicon, J. Appl. Phys. 67 (1990) 6764–6771.
 - [40] L. J. Geerligs, D. Macdonald, Dynamics of light-induced feb pair dissociation in crystalline silicon, Appl. Phys. Lett. 85 (2004) 5227–5229.
 - [41] F. E. Rougieux, C. Sun, D. Macdonald, Determining the charge states and capture mechanisms of defects in silicon through accurate recombination analyses: A review, Solar Energy Materials and Solar Cells 187 (2018) 263 – 272.
 - [42] A. A. Istratov, H. Hieslmair, E. Weber, Iron and its complexes in silicon, Applied Physics A: Materials Science & Processing 69 (1999) 13–44.
 - [43] O. Breitenstein, Understanding the current-voltage characteristics of industrial crystalline silicon solar cells by considering inhomogeneous current distributions, Opto–Electronics Review 21 (2013) 259–282.
 - [44] K. Yu, J. Liang, B. Qu, X. Chen, H. Wang, Parameters identification of photovoltaic models using an improved JAYA optimization algorithm, Energy Conversion and Management 150 (2017) 742–753.
 - [45] O. Y. Olikh, O. V. Zavhorodnii, Modeling of ideality factor value in n^+-p-p^+ -si structure, Journal of Physical Studies 24 (2020) 4701.
 - [46] F. Chollet, Deep Learning with Python, Manning, second edition, 2017.